JACS
JOURNAL OF THE AMERICAN CHEMICAL SOCIETY
pubs.acs.org/JACS
Article

In Situ Identification of Reaction Intermediates and Mechanistic Understandings of Methane Oxidation over Hematite: A Combined Experimental and Theoretical Study

Yulian He,[⊥] Facheng Guo,[⊥] Ke R. Yang,* Jake A. Heinlein, Scott M. Bamonte, Jared J. Fee, Shu Hu, Steven L. Suib, Gary L. Haller, Victor S. Batista,* and Lisa D. Pfefferle*

Cite This: *J. Am. Chem. Soc.* 2020, 142, 17119−17130
Read Online

ABSTRACT: Effective methane utilization for either clean power generation or value-added chemical production has been a subject of growing attention worldwide for decades, yet challenges persist mostly in relation to methane activation under mild conditions. Here, we report hematite, an earth-abundant material, to be highly effective and thermally stable to catalyze methane combustion at low temperatures (<500 °C) with a low light-off temperature of 230 °C and 100% selectivity to CO_2. The reported performance is impressive and comparable to those of precious-metal-based catalysts, with a low apparent activation energy of 17.60 kcal·mol^{-1}. Our theoretical analysis shows that the excellent performance stems from a tetra-iron center with an antiferromagnetically coupled iron dimer on the hematite (110) surface, analogous to that of the methanotroph enzyme methane monooxygenase that activates methane at ambient conditions in nature. Isotopic oxygen tracer experiments support a Mars van Krevelen redox mechanism where CH_4 is activated by reaction with a hematite surface oxygen first, followed by a catalytic cycle through a molecular-dioxygen-assisted pathway. Surface studies with *in situ* diffuse reflectance infrared Fourier transform spectroscopy (DRIFTS) and density functional theory (DFT) calculations reveal the evolution of reaction intermediates from a methoxy CH_3−O−Fe, to a bridging bidentate formate b-HCOO−Fe, to a monodentate formate m-HCOO−Fe, before CO_2 is eventually formed via a combination of thermal hydrogen-atom transfer (HAT) and proton-coupled electron transfer (PCET) processes. The elucidation of the reaction mechanism and the intermediate evolutionary profile may allow future development of catalytic syntheses of oxygenated products from CH_4 in gas-phase heterogeneous catalysis.

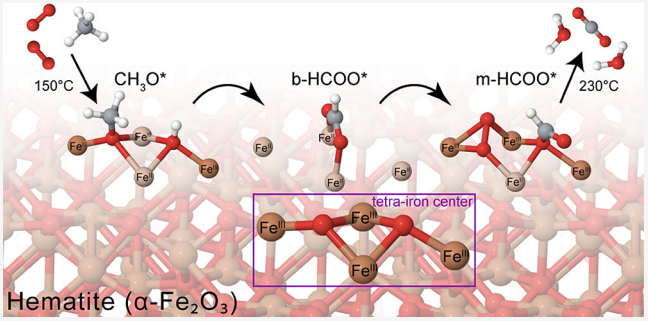

■ INTRODUCTION

Methane is the main constituent of natural gas (>90%), increasingly exploited as a popular alternative to the conventional fossil fuels since the shale revolution.[1,2] This perspective is largely driven by both the significant economic benefits of utilizing rather inexpensive and abundant CH_4 gas, and the rationality of partially reducing greenhouse gas emissions since methane produces the lowest amount of CO_2 per unit energy produced.[3] A natural-gas-powered vehicles (NGVs) program launched in Europe is an example of initiatives for using natural gas as a fuel in place of conventional gasoline or diesel. However, the environmental merits of the NGVs are jeopardized if unburned CH_4 is released by the exhaust since methane is a dangerous greenhouse gas with a global warming potential 86 times higher than CO_2 over 20 years.[3] Therefore, there is an urgent need for remediation of unburned CH_4 to fulfill the strict emission regulations of combustion at low temperatures (<500−550 °C), including approaches like catalytic methane combustion (CMC) described in eq 1.[4,5] CMC also has great potential as an alternative to conventional flame combustion in green power generation processes, such as in the natural-gas-powered gas turbines, where the operation temperatures are much lower and fewer harmful air pollutants such as NO_x, CO, and SO_x, are produced.[6]

$$CH_4(g) + 2O_2(g) \rightarrow CO_2(g) + 2H_2O(g)$$
$$\Delta H_r^\circ(298\ \mathrm{K}) = -803\ \mathrm{kJ{\cdot}mol^{-1}} \quad (1)$$

Methane activation is one of the main obstacles for any oxidation reaction, be it methane to methanol or catalytic combustion, due to the high degree of structural symmetry and low polarity of the methane molecule, which renders both

Received: July 3, 2020
Published: September 16, 2020

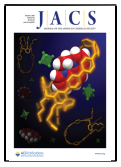

nucleophilic and electrophilic attacks on CH_4 rather challenging.[2,7] The most common activation pathway is through thermal, homolytic C−H bond cleavage using heterogeneous catalysts, where the hydrogen atoms can transfer to neighboring atoms in auxiliary reactions thus promoting the dissociative adsorption of CH_4 via the so-called thermal hydrogen-atom transfer (HAT) process.[8,9] So far, palladium-based catalysts have attracted the most attention for the CMC reaction with effective conversion at relatively low temperatures (below 550 °C). However, their high cost, low water poisoning resistivity, reduction at high temperature, and redispersion upon reoxidation have motivated the search for alternatives based on earth-abundant elements, such as single metal oxides, spinels, and perovskites.[4,10,11] The variable oxidation states of the transition metals in these oxides enable a redox cycle in the catalytic oxidation reactions by the release and restoration of the lattice oxygens. However, very few of them are reported capable of activating methane initially, thus hindering any subsequent conversion. Notable exceptions are supported CuO,[12] spinel oxide Co_3O_4,[4] MnO_x,[8] and perovskite $LaSrCuO_4$,[13] among others. Most of these materials, however, despite some promises, have not been as economically attractive as that of Pd-based systems due to their complicated catalyst structures, high catalyst mass loadings, small space velocity, or extremely lean fuel feed conditions. In addition, the understandings of their mechanisms of CH_4 activation remain less explored and controversial, making them worthwhile to investigate as they would be of great value not only for the CMC reaction but also for the broader methane conversion community.

Recently, iron oxides have shown promise as active catalysts for methane conversion reactions as they are analogous in functionality to the active sites in the enzyme methane monooxygenase, which converts methane to methanol in nature.[14,15] Over the centuries, iron oxides have gained a reputation in the catalysis community as an earth-abundant, nontoxic, and excellent performing catalyst for many important industrial processes, such as the Fischer−Tropsch synthesis, the Haber process, and the water−gas shift reaction.[16,17] However, their potential in methane conversion via heterogeneous catalysis has been quite limited to partial oxidation reactions such as to methanol[18] or to formaldehyde,[19] for instance, over Fe/ZSM-5 catalysts, where the active center was found to be the FeO^+ oxide species.[18,20] The complete oxidation route of methane as well as the fundamental activation mechanism is whereas studied to a much lesser extent.

Here, we find that hematite (α-Fe_2O_3), the most thermodynamically stable form of iron oxides, is a highly effective catalyst for the complete oxidation of methane with excellent stable performance below 500 °C in both nano and bulk forms, a low light-off temperature of 230 °C, and 100% selectivity to CO_2. From a molecular level, our theoretical analysis shows the catalytic active center is a tetra-iron structure with an antiferromagnetically coupled iron dimer on the (110) surface of hematite, analogous to that of the iron dimer active site of the soluble methane monooxygenase enzyme. In addition to its interest for CMC, the (110) facet of hematite has been reported to be an effective catalyst for other important oxidation processes such as water[21] and CO oxidation,[22] so we anticipate our findings would be of interest for these oxidative reactions as well as beyond methane oxidation. We report the study of the individual roles of lattice oxygens and oxygens from the gas phase based on isotopic oxygen tracer experiments to elucidate the reaction mechanism. We find a Mars van Krevelen type of redox mechanism with participation of the surface oxygen sites, supported by both experimental and theory. In addition, *in situ* diffused reflectance infrared Fourier transform spectroscopy (DRIFTS) on a designed 2D hematite catalyst with a large surface area shows vibrational signatures of surface intermediates, revealing a reaction pathway that evolves from methoxy to bridging bidentate formate, to monodentate formate, and finally to CO_2 as the temperature is increased. Density functional theory (DFT) modeling supports such a reaction pathway with favorable energetic changes via both thermal HAT and proton-coupled electron transfer (PCET) processes as well as calculated IR frequencies of the proposed intermediate surface species consistent with our *in situ* observations. This reported combination of experimental and theoretical analysis allows elucidation of the full mechanism of CH_4 oxidation over hematite, where a preactivation process first occurs by reaction with the surface lattice oxygens at lower temperatures, followed by a catalytic cycle through a molecular-oxygen-assisted pathway at higher temperatures.

■ EXPERIMENTAL SECTION

All chemicals used here were purchased from Sigma-Aldrich with purity ≥ 97%. Ultra-high-purity (UHP)-grade gases were purchased from Airgas.

Synthesis of Hematite Nanosheets. The synthesis of 2D hematite is described in detail in our previous work.[16,23] Typically, a rigid 2D material CuO nanosheet obtained from a soft templating process was used to hard template the growth of the ultrathin graphene-like hematite nanosheets via a redox reaction at the interface. The template was later removed by excessive washing with ammonium hydroxide and the precipitate was annealed at 400 °C for 30 min to form hematite nanosheets. The powder was finely crushed using mortar and pestle before further measurements.

Methane Catalytic Combustion. CMC reactions were performed using a flow reactor set up as schematically shown in Figure S1. Mass flow controllers and *k*-type thermocouples were used to control gas flow rates and temperature, respectively. Typically, 30.0 mg of catalyst was loaded into a straight tube quartz reactor and heated from 100−500 °C at 10 °C·min^{-1}. The total volumetric gas flow rate Q was 100 mL·min^{-1}, and the inlet feed composition was 5% CH_4 ((weight hourly space velocity (WHSV) = 10 000 mL·g^{-1}·h^{-1}), 20% O_2, and 75% Ar. The reaction was normally repeated in triplicate with the standard deviation noted in the figures. To quantify the conversion, the outlet gas composition was compared to the respective measurements of the prereaction steady state mass spectrometer signal. Using eq 2, the conversion was calculated at each point. Measurements were taken approximately every 3 s. The operating pressure was 1 atm, and no change in Argon signal was observed indicating that the pressure in the chamber remained constant. The reaction stoichiometry was calculated as suggested by eq 34, where PP stands for partial pressure and RSF is the relative sensitivity factor of the mass spectrometer for a specific mass to charge ratio. The stability test was performed at 500 °C for over 10 h under proportional-integral-derivative mode instead of ramping.

$$\%\text{X conversion} = \left(1 - \frac{\text{Measured X signal}}{\text{Prereaction X signal}}\right) \times 100\% \tag{2}$$

$$\frac{\eta_{O_2}}{\eta_{CH_4}} = \frac{\eta_{O_2}(\text{reacted})}{\eta_{CH_4}(\text{reacted})} = \frac{\%O_2\ \text{conversion} \times Q_{O_2}}{\%CH_4\ \text{conversion} \times Q_{CH_4}} \tag{3}$$

https://dx.doi.org/10.1021/jacs.0c07179
J. Am. Chem. Soc. 2020, 142, 17119−17130

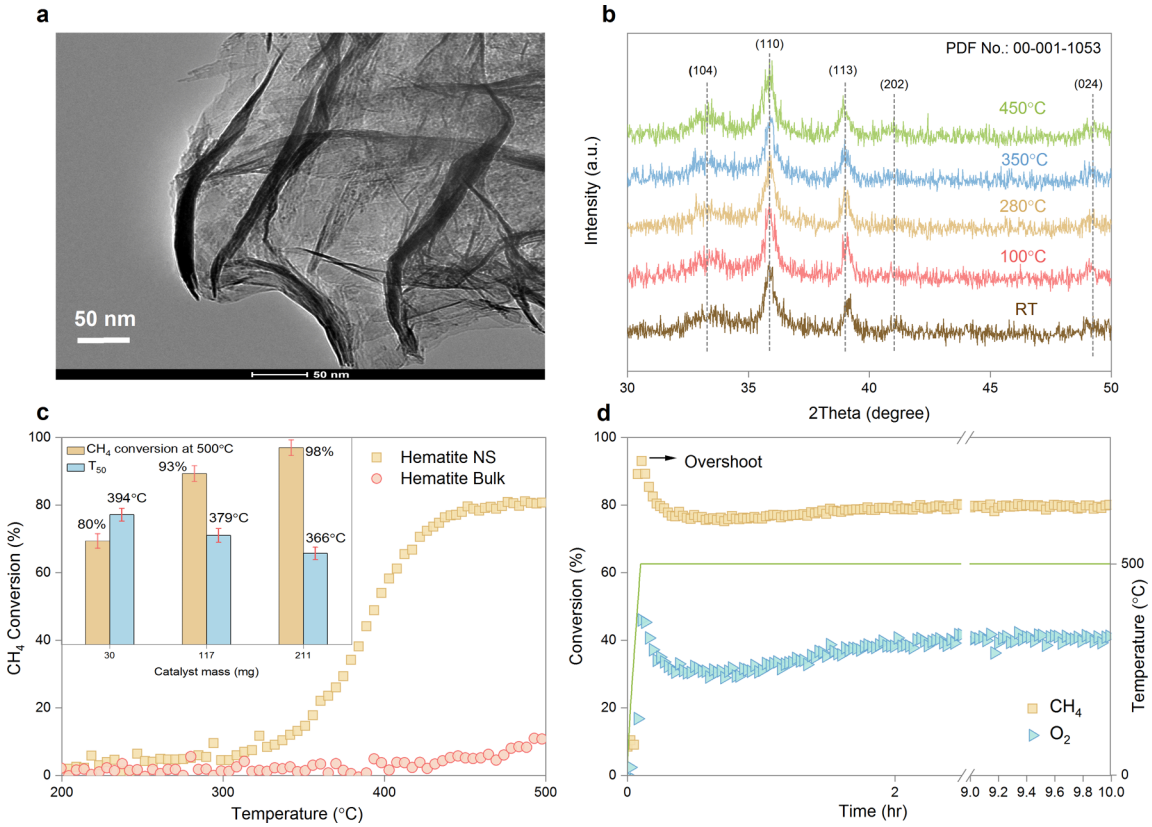

Figure 1. (a) TEM image showing the ultrathin structure of hematite nanosheets. (b) Diffraction patterns of hematite nanosheets agree well with the hematite standard (PDF No. 00−001−1053, JCPDS). *In situ* XRD analyses on hematite nanosheets at different reaction temperatures show no obvious changes both in the diffraction patterns and peak broadenings during the entire combustion experiment. (c) CH_4 conversion of hematite nanosheets versus bulk upon 30.0 mg as a function of temperature in CMC experiment with 5% CH_4 (WHSV = 10 000 mL·g^{-1}·h^{-1}) and 20% O_2 balanced with 75% Ar. The inset shows CH_4 conversion and T_{50} against catalyst mass loadings with standard deviations, the averaged conversions and T_{50} values are labeled on top of each column. (d) Stability test of 30.0 mg of hematite nanosheets at 500 °C over 10 h with negligible activity drop.

$$\frac{\eta_{H_2O}}{\eta_{CO_2}} = \frac{PP(H_2O)/RSF(H_2O)}{PP(CO_2)/RSF(CO_2)} \quad (4)$$

Isotopic Tracer Experiments. Temperature-programmed isotopic oxygen exchange (TPIOE) experiments and isotopic oxygen tracer experiments were performed using the same reactor set up as the methane catalytic combustion reaction. The isotopic oxygen balanced with He with a concentration ratio of $^{18}O_2$/He = 1:24 was purchased from Cambridge Isotope Laboratories, Inc. All parameters were kept the same except for changes in the inlet feed compositions: $^{18}O_2$/He/Ar = 1:24:75 for TPIOE, CH_4/$^{18}O_2$/He = 1:4:96 molar ratios for the tracer experiment. For both reactions, 30.0 mg of catalyst was used, and the total flow rate was 50 mL·min^{-1}, so the WHSV of CH_4 was set as 10 000 mL·g^{-1}·h^{-1}, the same as the combustion experiment.

CH_4-Temperature-Programmed Reduction (TPR). CH_4-TPR was performed using the same reactor set up, using 5% CH_4 (WHSV = 10 000 mL·g^{-1}·h^{-1}, the same as the combustion experiment) and 95% Ar. The gas mixture was introduced to 30.0 mg of hematite nanosheets and heated to 500 °C at 10 °C·min^{-1}.

***In Situ* X-ray Diffraction (XRD).** *In situ* XRD diffraction patterns were collected through Thermo-ARL X'TRA using Cu Kα radiation equipped with an Anton-Parr XRK-900 *in situ* reactor chamber. The same composited gas (CH_4/O_2 = 1:4 balanced with Ar) was introduced over 30.0 mg of the catalyst with a consistent space velocity as the catalytic measurements. Data analysis was performed using PDXL-2 Rigaku software.

In Situ DRIFTS Spectroscopy. The *in situ* FTIR studies were performed on a Nicolet 6700 FT-IR along with a DRIFTS chamber from Pike technologies. A ZnSe window was used for the reaction and the data was collected by a liquid-nitrogen-cooled MCT detector at 256 scans and 2 cm^{-1} resolution. For the measurements, 20 mg of iron oxide nanosheets was placed in a ceramic crucible and pretreated at 130 °C in argon for 1 h in the DRIFTS chamber to remove any surface impurities. The composite gas (CH_4/O_2 = 1:4 balanced with Ar) was introduced with similar space velocities as the catalytic combustion experiment, and the background spectra was taken before temperature ramping. The temperature was then increased at 10 °C·min^{-1} and multiple spectra were taken over 30 min for each temperature.

Calculations. All DFT calculations were performed with Vienna *Ab initio* Simulation Package[24−27] (VASP) version 5.4.1 based on periodic boundary spin polarized DFT+*U* calculation. We used Jmol version 14.30.2[28] for visualization and Adobe After Effect version 17.0.6 for animation. The Perdew−Burke−Ernerhof exchange-correlation functional[29] was used in conjunction with the projected augmented-wave method[30,31] to describe the electron−ion interactions. To properly describe the highly correlated 3d electrons in Fe ions, we used the DFT+*U* implemented in VASP following Dudarev's approach[32] to add on-site potentials to the d electrons of Fe. A value of 4.0 eV was used for the $U_{eff} = U - J$ parameter of Fe and 0.0 eV for all other elements according to Rollmann's *first-principles* calculations.[33] The Gaussian smear was used with the smearing parameter σ = 0.1 eV. The energy convergence criterion was set to be 10^{-4} eV per unit cell. For the optimization of the bulk hematite structure, the cutoff energy of the plane wave basis was chosen to be 450 eV. A Monckhorst−Pack type *k*-point grid of 3 × 3 × 3 was chosen for the bulk structure optimization. Both the unit cell and atomic positions were allowed to relax during the geometry optimization. The

https://dx.doi.org/10.1021/jacs.0c07179
J. Am. Chem. Soc. 2020, 142, 17119−17130

geometry optimization of bulk structure was finished when the energy difference between two consecutive calculations is less than 10^{-3} eV.

The hematite (110) facet model was generated from a 2 × 2 × 1 super cell of the optimized α-Fe_2O_3 bulk structure. For all the geometry optimization of slabs and molecules, we increased the cutoff energy of the plane wave basis to 520 eV. The force convergence criterion was set at 0.01 eV·Å^{-1}, and the maximum optimization step-size was 0.4 Bohr. Hematite is an antiferromagnetic system in a rhombohedral structure. The spins of Fe^{3+} ions are parallel within the (111) plane and antiparallel in other adjacent planes (Figure S15).[34] The antiferromagnetic property of hematite is modeled based on spin-polarized DFT+U theory. The reduction/oxidization states of Fe are described by different initial magnetic moment parameters (Table S2) based on Liao's benchmark.[35] The atomic boundary is defined by the Wigner−Seitz radius. A 3 × 1 × 3 Monckhorst−Pack type k-point grid was used to sample the Brillouin zone during the geometry optimization. The unit cell with dimensions of 8.76 Å × 25.12 Å × 13.83 Å with rich oxygen termination was used to model the α-Fe_2O_3 (110) facet, and an additional H parking slab with the same dimensions as the reaction site unit cell was also implemented in the calculations for the preactivation process to protect the reaction slab from over-reduction. The reaction slab contains four layers of Fe in total: The bottom two layers were frozen at their bulk positions, while the top two layers, as well as the molecules from the gas phase, were allowed to relax during geometry optimizations.

We also used the nudged elastic band (NEB) method[36] to get the hydrogen transition states' potential energy surface. NEB employed total 6 intermediate geometries with force convergence criterion set to be at 0.05 eV·Å^{-1}. The relative electronic energy ΔE were calculated according to eq 5

$$\Delta E = \sum E_{\text{product}} - \sum E_{\text{reactant}} \tag{5}$$

where $\sum E_{\text{product}}$ and $\sum E_{\text{reactant}}$ stand for the total electronic energies of products and reactants, respectively.

The frequency calculations were performed with VASP as well, and all of the parameters were kept the same for the optimization except for a higher energy convergence criterion at 10^{-5} eV per unit cell. A step-size of 0.015 Bohr was used in the finite different calculations to obtain the numerical Hessian in frequency calculations.

All coordinates of optimized structures can be found in the supporting VASP output ZIP file. Other characterization details on electron microscopies, X-ray photoelectron spectroscopy, and N_2-physisorption can be found in the Supporting Information.

■ RESULTS AND DISCUSSION

Structure Composition. The 2D hematite nanosheets are synthesized through a hard-templating wet-chemical route as extensively described in our previous work.[16,23] They resemble a graphene-like structure (Figure 1a) with an ultrathin thickness of 4−7 nm from our previous microscopic studies. X-ray diffraction patterns of the nanosheets match well with the hematite standard (Powder Diffraction File (PDF) No. 00−001−1053, Joint Committee on Powder Diffraction Standards (JCPDS)), with notable peak broadening caused by small crystallite sizes (Figure 1b). The 2D hematite nanosheets possess a high surface area value of 160 ± 5.5 m^2·g^{-1} (measured by N_2-physisorption, see characterization details in the Supporting Information) and a small average particle size of 37.3 ± 1.3 nm.

Catalytic Performance. In our CMC experiments, 5% CH_4 (WHSV = 10 000 mL·g^{-1}·h^{-1}), 20% O_2, and 75% Ar composite gases were flown over 30.0 mg of 2D hematite catalysts. Detailed descriptions on the reaction conditions and reactor setups can be found in the Experimental Section and Figure S1. The catalytic performance is shown in Figure 1c in yellow squares, with a light-off temperature as low as 230 °C, a maximum CH_4 conversion of 80% at 450 °C and 100% selectivity to CO_2: No byproducts such as H_2, CO, HCHO, HCOOH, and CH_3OH were detected in the complete mass spectra shown in Figure S2. A self-dehydration behavior (Figure S2) was also observed prior to the onset of the reaction near 100 °C, which is likely associated with the dehydration of the surface hydroxyl groups from the hematite structure. The combustion reaction proceeded with a stoichiometric ratio of $\frac{\eta_{O_2}}{\eta_{CH_4}} = \frac{\eta_{H_2O}}{\eta_{CO_2}} = 2$ as calculated by eqs 3 and 4 in the Experimental Section and shown in Figure S3, consistent with the stoichiometric complete oxidation of methane. In a blank test without any catalyst, no activity was observed in this temperature range (Figure S4). The plateau of activity above 400 °C is caused by the amount of catalyst used under such a high WHSV and can be mitigated by increasing the catalyst mass loadings (see the light-off curve in Figure S5), accompanied by a simultaneous shift of half-conversion temperatures (T_{50}) toward lower values as shown in the Figure 1c (inset) or by lowering the total flow rate/WHSV to increase the catalyst contact time (data not shown). However, the lower catalyst loading, 30.0 mg, and this sufficiently high flow rate/WHSV were chosen as more appropriate parameters for kinetic analyses to avoid diffusion limitations. We note that the catalytic performance with such a low mass loading/high WHSV, corresponding to a specific reaction rate of 62.00 mmol·g^{-1}·s^{-1} at T_{50}, is truly outstanding for a simple metal oxide structure. Most previously reported specific rates of similar unsupported oxide systems, like $NiCo_2O_4$ and MnO_2,[4,37] are almost 1 order of magnitude lower than that of this work. It even outperforms many supported Pd catalysts and bimetallic Pd/Pt and Au/Pd systems in terms of specific rate and apparent activation energy (*vide infra*).[38,39] A comprehensive comparative table with some typical catalytic systems and the justifications of such comparison between supported and nonsupported systems are given in Table S1.

As a control, bulk hematite with only one-thirtieth the surface area (5.38 ± 0.35 m^2·g^{-1}) of that of the 2D structure and an average particle size of 1.16 ± 0.11 μm was also tested, giving a much lower activity (up to 11% at 500 °C) and a significantly higher light-off temperature (∼400 °C) upon the same mass loading of 30.0 mg (Figure 1c). However, when increasing its mass loading to reach a similar total surface area, 900.0 mg of bulk hematite showed comparable activity to the 2D nanosheets (Figure S6), implying that hematite is reactive in both bulk and nano forms, while in the interest of surface studies, 2D hematite is more attractive overall due to its large surface area and high density of active sites per unit mass.

In situ XRD analyses performed across the entire reaction temperature range barely show changes in either the diffraction patterns or the peak broadening (Figure 1b), implying excellent preservation of the chemical composition and particle size of the hematite nanosheets during the CMC reaction. In addition, the nanomorphology was kept almost intact from postreaction TEM/SEM analyses (Figure S7) and X-ray photoelectron spectroscopy (XPS) measurements barely showed any changes at Fe 2p before and after the reaction (Figure S8), where the oxidation state of Fe and the surface atomic ratio of Fe/O = 2:3 remained consistent. Furthermore, the stability was also maintained when the reaction was brought to 500 °C rapidly (within 6 min) and kept constant for over 10 h upon 30.0 mg catalyst loading (Figure 1d). While under this fast temperature increase, the CH_4 conversion first

https://dx.doi.org/10.1021/jacs.0c07179
J. Am. Chem. Soc. 2020, 142, 17119−17130

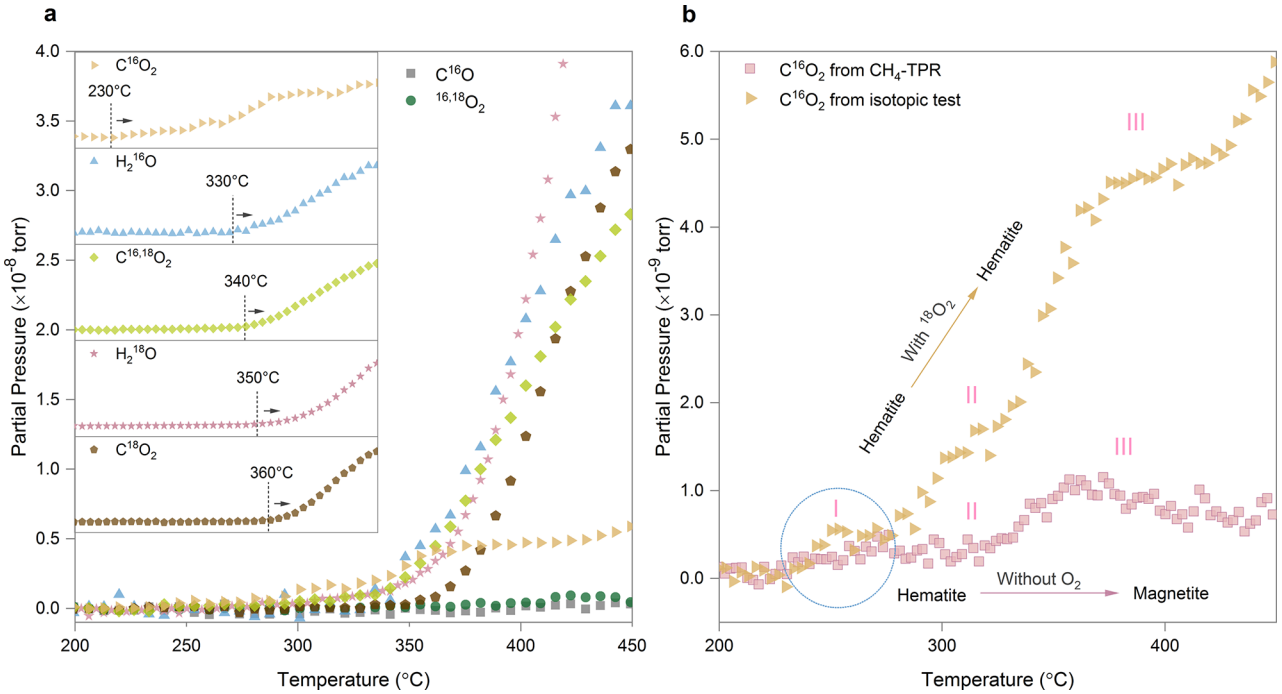

Figure 2. (a) Species evolution profile of hematite nanosheets in the isotopic oxygen tracer experiment with a gas feed composition of $CH_4/^{18}O_2/He$ = 1:4:96, WHSV = 10 000 mL·g^{-1}·h^{-1} for CH_4. He was used instead of Ar as the carrier gas here as the purchased $^{18}O_2$ was balanced by He gas initially. (b) Multistage activation behaviors between lattice oxygens and CH_4 with (refers to isotopic experiment) or without (CH_4-TPR) additional oxygen in the gas phase. The gas feed for CH_4-TPR is 5% CH_4 balanced by Ar with a WHSV = 10 000 mL·g^{-1}·h^{-1} for CH_4. The first stage activation is similar in both cases, but the rate deviates afterward given the difference in ability to maintain the active hematite structure.

soared up to 94%, then dropped to below 80%, and finally, as the temperature stabilized, the conversion equilibrated at 80%. This overshoot is likely due to the heat released from the combustion reaction itself accumulated in such a short period of time, resulting in a higher local temperature and thus higher conversion than that from the ramping test. After the steady state was reached, the activity was well-maintained over 10 h with a negligible drop.

The apparent activation energy was calculated by constructing an Arrhenius plot from isothermal experiments at various temperatures with CH_4 conversion below 10% to avoid diffusion limitations. The apparent activation energy calculated from the slope of the Arrhenius plot is 17.60 ± 1.34 kcal·mol^{-1} (Figure S9), which is significantly lower than that of a typical metal oxide catalyst, for which the apparent activation energy falls between 19 and 35 kcal·mol^{-1}.[8] This value is even comparable to that of most reported Pd-based catalysts, whose apparent activation energies are in the 17−20 kcal·mol^{-1} range for crystalline PdO and in the 40−45 kcal·mol^{-1} range for metallic Pd.[8,40,41] Justification of such a low apparent activation energy requires investigation into the reaction fundamentals from *in situ* spectroscopies, in conjunction with theoretical analyses at a molecular level, as discussed in the following sections.

Reaction Model. The reaction models of metal oxide-based catalysts remain controversial in the CMC community, as well as more broadly in hydrocarbon combustion studies. Four types of reaction models are typically proposed as schematically illustrated in Figure S10, including the following: (1) the Langmuir−Hinshelwood (LH) model, where the surface reaction occurs through the dissociative/molecular adsorption of oxygen and adsorption of methane, (2) the Eley−Rideal (ER) model, where the reaction occurs between dissociatively adsorbed oxygen and gaseous methane, (3) the Mars van Krevelen (MvK) redox model, where the reaction occurs through the alternating reduction and oxidation of the catalyst surface, and (4) the two-term model (TT), where oxidation on the catalyst surface takes place by two routes, via the lattice oxygen and via the adsorbed oxygen.[8] The controversy is mainly resulting from the complexity introduced by the multiple oxygen sources of both the metal oxide lattices and the molecular dioxygen from the gas phase. To elucidate the reaction model, we designed isotopic oxygen tracer experiments that resolve the contributions from the different oxygen sources.

The CMC reaction was again conducted by flowing isotopic $^{18}O_2$ instead of $^{16}O_2$ without disturbing other parameters. The oxygen kinetic isotopic effect could be neglected as the reaction order with respect to oxygen is zero.[42] The resulting isotopic tracer mass spectra are shown in Figure 2a, with light-off behavior similar to that of the ordinary combustion experiment. However, most notably, with the reaction initiated at 230 °C, $C^{16}O_2$ was produced first, followed in a distinct order by $H_2{}^{16}O$, $C^{16,18}O_2$, $H_2{}^{18}O$, and finally $C^{18}O_2$ (Figure 2a inset). During the entire tracer experiment, there was negligible amount of $^{16,18}O_2$ species detected in the gas phase, suggesting no exchange of lattice ^{16}O to the gas phase in the temperature range of our experiment. Nevertheless, metal oxides are known for undergoing oxygen-exchange at gas−solid interfaces at elevated temperatures. For methane combustion in particular, several authors have proposed the occurrence of an oxygen-exchange reaction prior to the increase of catalytic activity.[43] An additional control experiment using TPIOE test, however, showed the lattice oxygen ^{16}O diffusion to the gas phase did not start below 400 °C (Figure S11). These findings suggest that the oxygen-exchange behavior in fact occurs later than the

https://dx.doi.org/10.1021/jacs.0c07179
J. Am. Chem. Soc. 2020, 142, 17119−17130

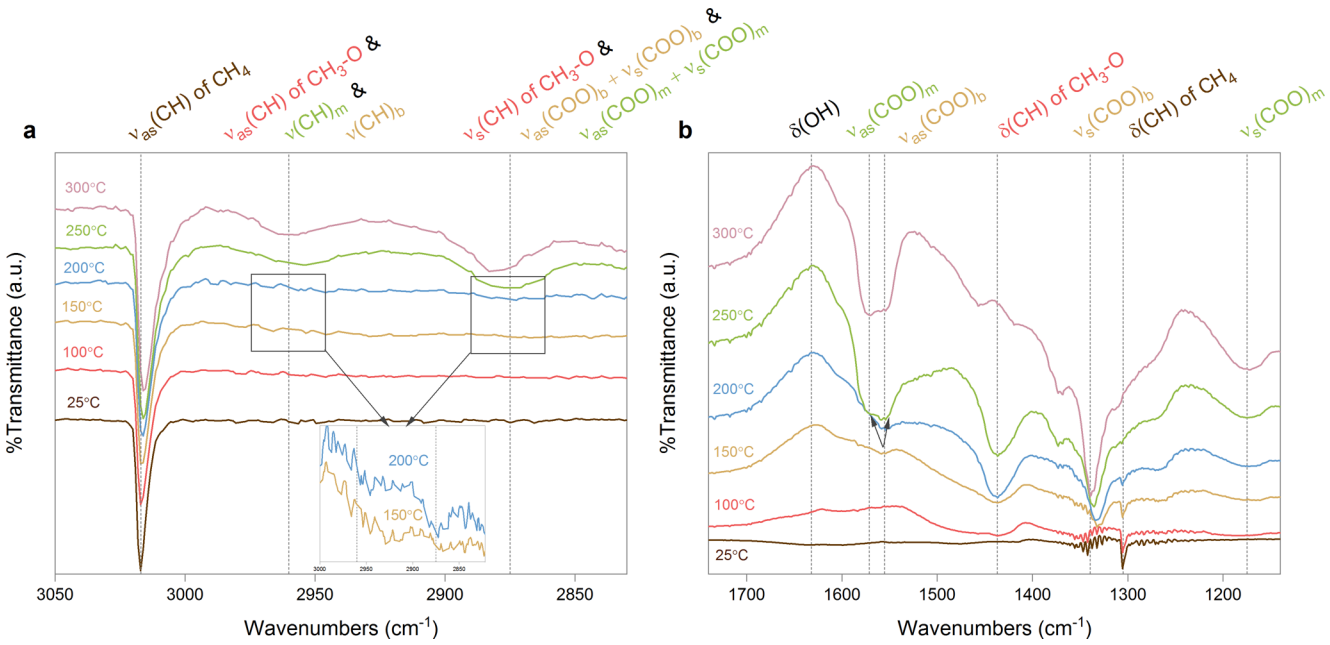

Figure 3. *In situ* DRIFTS spectra with species assignments labeled on top, WHSV of CH_4 = 10 000 mL·g^{-1}·h^{-1}. (a) C−H stretching of free CH_4, methoxy and formate species together with the combination modes of formate. (b) Fingerprint region showing the C−H bending of free CH_4 and methoxy as well as the paired carbonyl (COO) stretching of formate. The peak splitting of the antisymmetrical carbonyl splitting is characteristic of a bidentate formate transition to monodentate.

reaction initiation in our case, so the detected ^{16}O component in the products must only come from the lattice solid phase. This observation is consistent with the numerical analysis of the mass balance, showing that initially (T < 385 °C) the ratio $^{16}O/^{18}O$ > 1 in all oxygen-containing products, then $^{16}O/^{18}O$ ∼ 1 at T∼ 385 °C, and finally $^{16}O/^{18}O$ < 1 at T > 385 °C. This observed trend, in conjunction with the order for product formation mentioned above, strongly implies a predominant active role of the lattice oxygen at the reaction initiation of the reaction, ruling out both the LH and ER mechanisms, where the oxygen from the gas-phase $^{18}O_2$ would be the preferred oxidizing agent. Additionally, the prioritized formation of $C^{16}O_2$ over $C^{16,18}O_2$ also excluded the TT model where the mixed $C^{16,18}O_2$ species would have been preferentially formed instead. Therefore, the results are most consistent with a MvK redox mechanism with participation of the surface lattice oxygen as the initial oxidation step, forming lattice-oxygen-containing products $C^{16}O_2$ and $H_2{}^{16}O$. Then the catalyst surfaces are reoxidized by molecular dioxygen $^{18}O_2$ from the gas phase, producing a mixture of isotopic products including $C^{16,18}O_2$, $H_2{}^{18}O$, and $C^{18}O_2$. Similar mechanisms have also been proposed for other systems, including PdO[44] and Co_3O_4 spinel catalysts.[45] The deconvolution of reaction models using oxygen isotopes becomes more complex and difficult at temperatures which are >400 °C due to the oxygen exchange between the gas and solid phase, so we only focus our analyses before such exchange predominates.

A control experiment of a TPR reaction, where only CH_4 and Ar were flown, also supported a MvK redox mechanism (Figure 2b). In this test, hematite showed the ability of activating CH_4 in the absence of molecular dioxygen to produce CO_2, which is not expected for many other catalysts where CH_4 activation must occur through a molecular-dioxygen-assisted pathway,[2] again suggesting the participation of lattice oxygen in methane activation. A similar self-dehydration behavior was observed again here prior to the onset of the reaction (Figure S12). More information can be gleaned when comparing the $C^{16}O_2$ channel from the isotopic tracer experiment and the CO_2 channel from the CH_4-TPR (Figure 2b). In this comparison, both channels only reflect the interactions between the lattice oxygens and CH_4. For both scenarios, a multistage activation behavior was observed that is likely due to CH_4 reacting with different lattice oxygen made available by the increased lattice oxygen diffusion as the temperature was increased. In the first activation stage (circled in blue), both channels appeared similar to comparable initiation temperatures (230 °C) and partial pressures (yields), presumably associated with the similar reaction between the active surface oxygens and the adsorbed CH_4, while after the consumption of the first-generation surface oxygens, the reaction kinetics deviated. In the case of CH_4-TPR, the yields were much lower in the absence of external oxygen sources, as hematite was gradually reduced into magnetite by reacting with CH_4, as examined by XRD analysis (Figure S13). With additional oxygen from the gas phase, the catalyst surfaces can be quickly reoxidized following the MvK redox mechanism, so the hematite composition as well as the active centers can be well-maintained at all times during the combustion experiment, thus resulting in higher yields. Notably, in both scenarios, this observed multiple activation stage behavior is highly consistent in terms of temperature dependence, suggesting a similar interaction of methane with surface lattice oxygens regardless of the presence of molecular dioxygen, further supporting the active participation of lattice oxygen in the entire CMC reaction.

We also note the leveling off of the $C^{16}O_2$ channel and the much faster rates of producing ^{18}O-containing species at higher temperatures, compared to the ^{16}O counterparts, particularly $C^{18}O_2$ versus $C^{16}O_2$ (Figure 2a), with the ratio of $^{16}O/^{18}O$ < 1. An estimation of the ^{16}O mass balance at 450 °C using the ideal gas law gave a total ^{16}O consumption on the magnitude of 10^{-5} mol, taking up only a small percentage (∼2.6%) of the

https://dx.doi.org/10.1021/jacs.0c07179
J. Am. Chem. Soc. 2020, 142, 17119−17130

Table 1. Comparisons of Experimental and Theoretical Vibrational Frequencies of Important Reaction Intermediates

species	vibrational modes	experimental (cm^{-1})	theoretical (cm^{-1})[a]	temperature (°C)
CH_4	ν_{as}(CH)	3017	3100	25−300
	δ(CH)	1305	1284	
CH_3−O−Fe	ν_{as}(CH)	2930−2985	2986	150−250
	ν_s(CH)	2850−2900	2921	
	δ(CH)	1437	1463, 1447, and 1424[b]	
b-HCOO−Fe	ν(CH)	2930−2985	2985	150−300
	ν_{as}(COO) + ν_s(COO)	2850−2900	2903	
	ν_{as}(COO)	1555	1557	
	ν_s(COO)	1335	1345	
m-HCOO−Fe	ν(CH)	2930−2985	2976	250−300
	ν_{as}(COO) + ν_s(COO)	2850−2900	2799	
	ν_{as}(COO)	1572	1606	
	ν_s(COO)	1189	1193	

[a]Theoretical harmonic frequencies. [b]These three vibrational modes were ascribed to be distinct CH bending signals of methoxy species with small frequency difference; they may be all described by the broad peak at 1437 cm^{-1} observed experimentally.

total lattice oxygen (∼10^{-4} mol) loaded. Therefore, the leveling off of the $C^{16}O_2$ channel and the lower producing rates are likely not caused by the intrinsic concentration constraints, but more likely result from the slower reaction kinetics of lattice oxygen ^{16}O participation compared to the molecular oxygen ^{18}O at high temperatures. All discussions above point to a MvK redox mechanism with an initial lattice oxygen dominated participation and an increase of molecular oxygen participation as temperature increases.

Reaction Intermediates. Surface intermediates were probed by *in situ* DRIFTS measurements (Figure 3), where IR signals were collected over the hematite nanosheet surfaces in the temperature range of 25−300 °C under CMC reaction conditions. Multiple positive peaks were detected in the 3580−3750 cm^{-1} range (Figure S14a) and 1632 cm^{-1} (Figure 3b) above 100 °C, corresponding to the desorption of water (or −OH groups) formed upon self-dehydration and methane combustion.[46] Additionally, the paired negative peaks at 2300−2400 cm^{-1} (Figure S14b), detected above 200 °C, are typical of the P, Q, and R branches of the CO_2 in the gas phase.[47] Strong characteristic antisymmetric stretching ν_{as}(CH) and bending δ(CH) signals for free CH_4 molecules (Figure 3) were observed at 3017 and 1305 cm^{-1},[48] respectively, with intensities decreasing with temperature, indicative of CH_4 consumption. All these observations confirm once again the complete oxidation of CH_4 to CO_2 and H_2O, with no CO signal detected.

The paired peaks at ∼2960 and ∼2875 cm^{-1} along with the band at 1437 cm^{-1} detected above 150 °C correspond, respectively, to the characteristic ν(CH) asymmetric, symmetric stretch, and bending upon formation of methoxy species (−OCH_3).[46,49] Notably, the intensity of the bending peak first increased with temperature, then decreased, and finally disappeared at 300 °C (Figure 3b). This is likely to be the result of the increased CH_4 adsorption to form −OCH_3 as temperature rises, balanced with the simultaneous increase of the turnover rate to consume −OCH_3. While interestingly, the paired peaks at ∼2960 and ∼2875 cm^{-1} did not follow such a trend, but instead, intensified as temperature increased. These peaks above 200 °C are more likely associated with the ν(CH) and the combination modes of ν_{as}(COO) and ν_s(COO) from a formate species on metal oxide surfaces, formed by the subsequent oxidation of the methoxy intermediates.[50,51] The detection of the characteristic carbonyl stretching signals ν_{as}(COO) and ν_s(COO) at ∼ 1555 and 1335 cm^{-1} also supports the formation of formate.[52] In addition, the difference between the ν_{as}(COO) and ν_s(COO) peak centers was found to be approximately 220 cm^{-1}, typical of a bidentate formate configuration and distinguishable from other species such as surface carbonates.[52] More interestingly, the peak at 1555 cm^{-1} was separated into two components when the temperature further increased above 250 °C. This was observed previously in the transition from a bidentate formate to a monodentate formate due to the repulsion among the bidentate configurations at high concentration by Bell et al.[50,52] These findings strongly imply formation of a stable formate intermediate species on the surface of hematite nanosheets in the CMC reaction, with intermediate evolution from a methoxy, to a bidentate formate, and to a monodentate formate before CO_2 is finally formed as the temperature increases.

DFT calculations allowed us to validate our experimental frequency assignments at the molecular level. Structural models of the proposed intermediate species were built on a hematite (110) surface (*vide infra*), and all vibrational modes were carefully examined. Table 1 provides a detailed comparative analysis of experimental and theoretical vibrational bands. The IR vibrational frequencies of free CH_4 were used as reference for theory-based calculations to properly compare the theoretical and experimental findings. Their values matched well, so no scaling was required for the theoretical model. The theoretical calculations were found to be highly consistent with our experimental IR assignments. These results strongly support our analyses of the reaction intermediates, as described above. Video S1 includes animations for all the calculated vibrational modes along with the frequencies.

Reaction Mechanism. Upon the basis of the successful identifications of reaction intermediates *in situ* and their order of formations as a function of temperature, we applied DFT to rationalize the reaction mechanism of CH_4 oxidation over hematite at an atomic level, where the activation process first occurs with participation of the surface lattice oxygen, followed by a full catalytic cycle, with molecular dioxygen from the gas phase involved. The hematite (110) surface was chosen as the primary model since it is the most pronounced facet in the XRD pattern (Figure 1b), and it has been reported to be the most reactive plane for many catalytic oxidation reactions such

https://dx.doi.org/10.1021/jacs.0c07179
J. Am. Chem. Soc. 2020, 142, 17119−17130

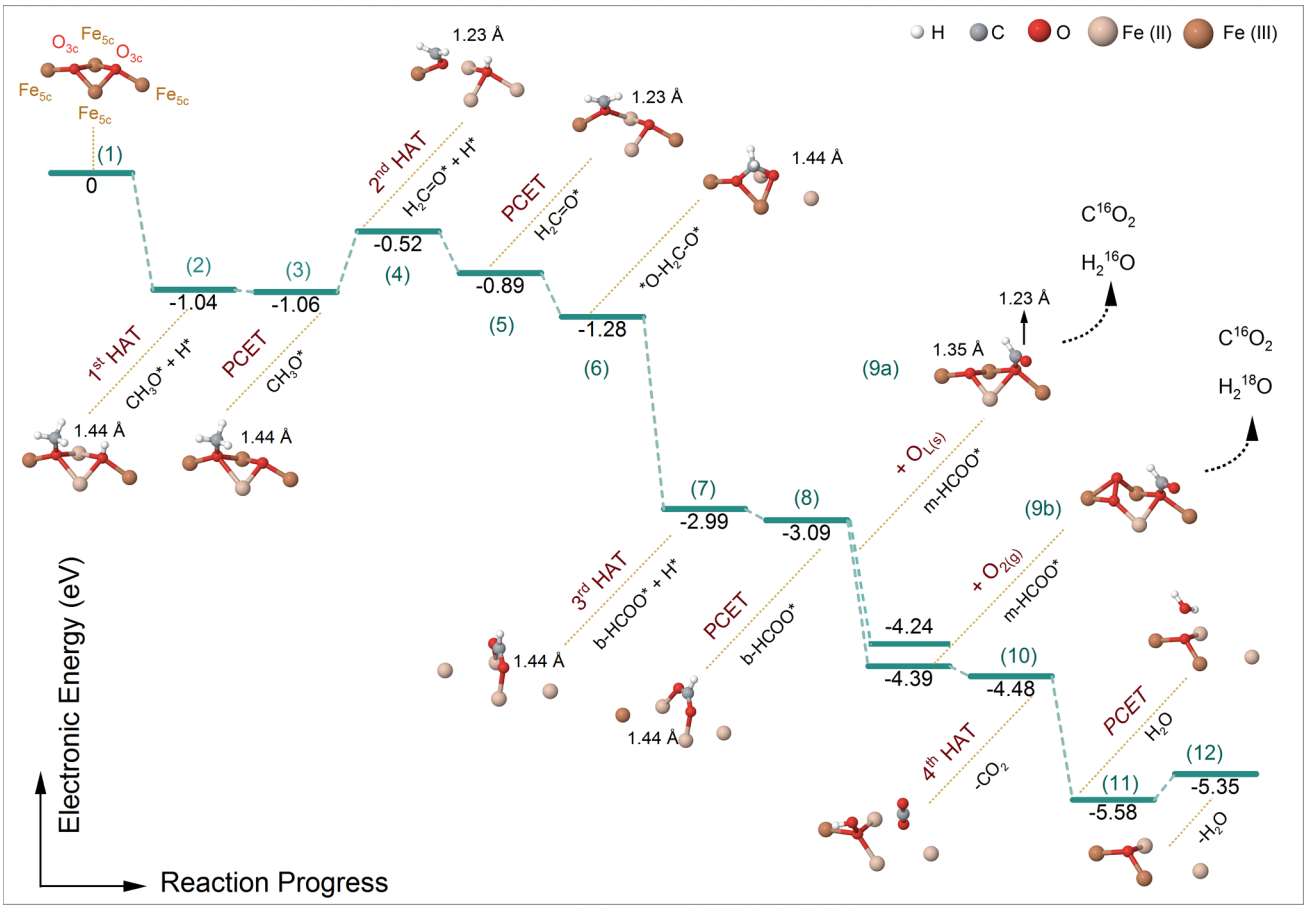

Figure 4. Proposed CH_4 preactivation process via lattice oxygen on hematite governing at low temperatures with calculated relative electronic energies according to eq 5. The overall reaction described here is hematite (110)(s) + CH_4(g) + O_2(g) → hematite (110)−O vacancy(s) + CO_2(g) + H_2O(g). HAT and PCET stand for thermal hydrogen-atom transfer and proton-coupled electron transfer process, respectively. The labeled C−O bond lengths of 1.44 and 1.23 Å are characteristic of a single and double bonds, respectively. The corresponding H atom parking situation for each model can be found in the Figure S17.

as water[21] and CO oxidation.[22] Most importantly, this facet possesses antiferromagnetic diiron oxo cores analogous to the diiron active site in the soluble methane monooxygenase enzyme, where CH_4 is activated to produce CH_3OH in nature,[15] although with a different Fe oxidation state and coordination environment (Figure S15).

Like most polar surfaces of metal oxides, the (110) surface of hematite is covered with hydroxyl groups due to dissociatively chemisorbed water molecules, which hinder the activation of CH_4 by blocking the surface active sites.[53] At elevated temperatures, the surface hydroxyl groups are eliminated by self-dehydration, an essential step for opening up the covalency of active sites and enable CH_4 adsorption. As we mentioned previously, this dehydration step was experimentally observed in our system prior to the onset of the combustion reaction. After self-dehydration (Figure S16), the model surface consists of two types of oxygens on the first two atomic layers, including a 3-coordinate O_{3c} and a 2-coordinate O_{2c} with a ratio of 2:1 and two types of 5-coordinate irons Fe_{5c} (two-thirds of which are bridged by two O_{3c}, while the rest are connected by one O_{3c} and one O_{2c}). The two adjacent Fe_{5c} atoms bridged by two O_{3c} possess opposite magnetic moments.[34] More electronic structure details can be found in "Calculation" section and Figure S15.

The complete oxidation process of CH_4 involves four hydrogen atom and eight electron transfers. We first considered the adsorption of CH_4 to the surface to simulate the reaction with dominant participation of lattice oxygen at lower temperatures (Figure 4). For clarity, we only show the reaction evolutionary profile at the proposed tetra-iron active core. An additional slab was used as a reservoir in conjunction to model H atom abstraction, as shown and justified in Figure S17, to avoid over-reduction of the reaction site. Interestingly, unlike many scenarios where lower-coordinate atoms are typically more reactive,[53,54] we find the most favorable adsorption site is on the two adjacent O_{3c} atoms (2.58 Å away from each other, the closest O−O distance on the surface), inducing formation of the methoxy intermediate (Figure 4, from (1) to (2)), with an adsorption energy of −1.04 eV and a C−O bond length of 1.44 Å. The comparison to binding energies for CH_4 adsorption on Fe and O_{2c} is provided in Figure S18. The stability is due to the favorable O−O distance of the two adjacent O_{3c} atoms as well as the antiferromagnetic characteristic of the bridged diiron couple, which favors dissociation of the C−H bond by keeping the total spin of the system intact (zero), therefore lowering the adsorption barrier. In this case, a possible CH_4 activation pathway is through homolytic bond cleavage by direct thermal HAT. According to that process (see details in Figure S19a), the lone-pair of electrons in the O_{3c} can conjugate with Fe_{5c} as a valence tautomeric transition to form oxygen-centered radical species, analogous to the commonly reported active site for

https://dx.doi.org/10.1021/jacs.0c07179
J. Am. Chem. Soc. 2020, 142, 17119−17130

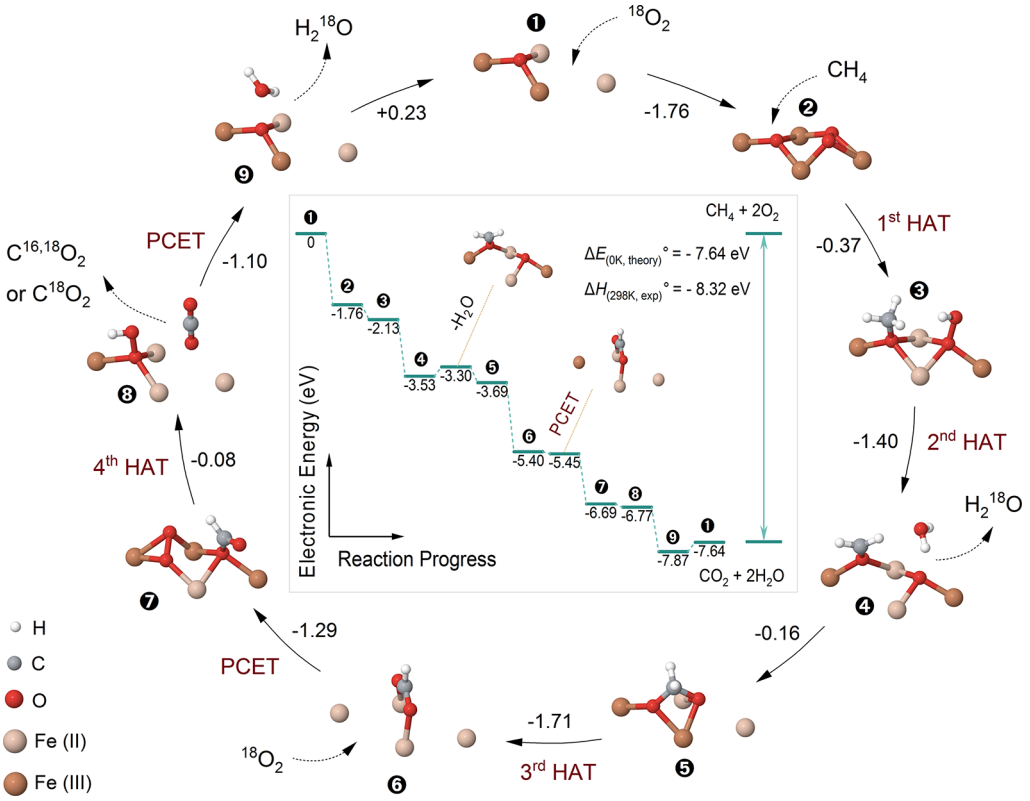

Figure 5. Proposed catalytic cycle for the CMC reaction at higher temperatures via molecular-oxygen-assisted pathway with calculated relative electronic energies according to eq 5. The overall reaction described here is $CH_4(g) + 2O_2(g) \rightarrow CO_2(g) + 2H_2O(g)$. The energy difference for this cycle equals the theoretical heat released by the CMC reaction at 0 K (−7.64 eV), and it is close to the standard heat of the reaction at 298 K. The omitted two steps in the cycle are the water desorption process between (4) and (5) with an energy cost of +0.23 eV, similar to that from (9) to (1), and an intended PCET process with negligible (−0.05 eV) energy difference between (6) and (7) due to the size constraint of the computational model. The numbers are in eV.

thermal activation of CH_4 via HAT in oxides gas-phase catalysis.[9] The indirect HAT pathway by metal mediation seems less likely, although the surface irons are unsaturated, as formation of the Fe−C bond (−376.3 ± 28.9 kJ·mol^{-1}) indirectly is much less favorable than that of a C−O bond (−1076.38 ± 0.67 kJ·mol^{-1}) following the direct route.[55]

The PCET process, where the electron and proton are transferred to different locations, was also analyzed as a mechanism to vacate the O_{3c} site for subsequent HAT activation of the adsorbed methane backbone. Both HAT and PCET can be rationalized with valence tautomerism. The underlying dependence of such dichotomic electron transfer processes was explained in great detail elsewhere by Usharani et al.[56] where H-abstraction occurred mostly by PCET for those MO−H bonds (M = transition metal), and by HAT for C−H bonds in similar iron oxo complexes. Consequently, the proton adsorbed on the O_{3c} can be transferred to a neighboring oxygen by PCET with a negligible energy change of −0.02 eV (Figure 4, from (2) to (3)), and the calculated energy barrier (0.85 eV) of such transfer process is sufficiently low for thermal catalysis (Figure S20). The transfer leaves the O_{3c} unoccupied and therefore facilitates the second C−H bond dissociation by HAT to form a formaldehyde-like moiety (Figure 4, from (3) to (4)), with a reduced C−O bond length of 1.23 Å characteristic of a double bond, C═O. The energy cost of this step (0.54 eV) is due to the rearrangement of Fe−O bonds necessary for the geometry change. After another PCET process (Figure 4, from (4) to (5), with energy change of −0.37 eV), the O_{3c} site is regenerated, with a lone pair of electrons on O_{3c} that reacts with the formaldehyde moiety through a nucleophilic attack (Figure 4, from (5) to (6) with energy change of −0.39 eV), cross-linking the two O_{3c} to form an acetal-like structure O−CH_2−O as during formaldehyde hydration when forming methylene glycol.[57] The detailed proposed electron transfer process is provided in Figure S19a. The O−CH_2−O bridging species is a precursor for formation of bidentate formate (Figure 4, from (6) to (7)), after the third HAT process on the carbon backbone. This process is very favorable, with an energy decrease of −1.71 eV, due to the structural stability of the bidentate intermediates which makes it easy to be probed by *in situ* DRIFTS measurements.

As the bidentate formate accumulates on the surface, transition from a bidentate bridging configuration to a monodentate coordination is expected due to replusion,[52] with an energy change of −1.30 eV (Figure 4, from (8) to (9)). The transition forms an oxygen vacancy that can be quickly replenished by either a neighboring lattice oxygen diffusion (Figure 4, from (8) to (9a), ΔE = −1.15 eV) or molecular dioxygen (Figure 4, from (8) to (9b), ΔE = −1.30 eV), both of which eventually lead to formation of $C^{16}O_2$ but different H_2O species. The lattice oxygen diffusion is consistent with the observed multistage activation behavior, as discussed earlier in Figure 2b. After the fourth HAT process and PCET (Figure 4, from (9) to (11)), CO_2 and H_2O are formed, leaving oxygen vacancies on the surface. Remarkably, the $C^{16}O_2$ was detected much earlier than $H_2{}^{16}O$ in the isotopic

https://dx.doi.org/10.1021/jacs.0c07179
J. Am. Chem. Soc. 2020, 142, 17119−17130

tracer experiment, which is consistent with the desorption of CO_2 being more favorable (Figure 4, from (9) to (10), with an energy change of −0.09 eV) than the desorption of water (Figure 4, from (11) to (12), with an energy change of +0.23 eV), which may cause water retention on the surface and therefore belated detection, as commonly observed in many other systems such as supported PdO catalysts.[58] Another observation is that the preactivation of CH_4 over hematite by participation of surface lattice oxygens leads to reduction of surface Fe(III) to Fe(II) as well as formation of O vacancies (Figure 4, from (1) to (12)). Therefore, in the absence of external oxygen source to replenish the vacancies, further reduction of the hematite to magnetite will occur, as is the case in the CH_4 TPR experiment (Figure 2b).

Formation of oxygen vacancies has been shown in many previous reports to facilitate both lattice oxygen diffusion and molecular dioxygen adsorption;[59] both processes will promote catalytic activity. In Figure 5, we evaluate the transition to the molecular-dioxygen-assisted regime at higher temperatures. With the oxygen vacancies formed after the preactivation process, the adsorption of molecular oxygen becomes more favorable with a calculated adsorption energy of −1.76 eV (Figure 5, from (1) to (2)). A peroxide bond is proposed to form, which assists the activation of CH_4 by a similar HAT process as proposed above to form methoxy species with an energy decrease of −0.37 eV (from (2) to (3)). The proposed activation pathway involving detailed electron transfer process is provided in Figure S19b. In this scenario, the total energy decrease for the dissociative adsorption of CH_4 is −2.13 eV (from (1) to (3)), which is much lower than that of the preactivation process (−1.04 eV) involving the surface lattice oxygen, consistent with the observation that as the vacancies accumulate at higher temperatures the ^{18}O isotope-containing products become dominant in our isotopic tracer experiment. In contrast, at lower temperatures, such vacancy structures are fewer, so CH_4 is primarily activated by lattice oxygen. In addition, the second HAT process (from (3) to (4)) via molecular oxygen assistance is calculated to be more favorable (−1.40 eV) than when assisted by lattice oxygen (+0.54 eV) due to the more favored geometry with breaking of fewer Fe−O bonds and the higher oxidation power of OOH over just the surface lattice O. The subsequent activation pathway (from (4) to (9)) is analogous to that proposed in the preactivation stage with similar intermediate evolutions and energy changes, leading to formation of isotope-containing products $C^{16,18}O_2$, $H_2{}^{18}O$, and $C^{18}O_2$. After desorption of all products, the active center eventually goes back to the initial vacancy structure (from (9) to (1)) to restart the catalytic cycle. The overall electronic energy change (−7.64 eV) in the cycle is equivalent to the theoretical energy difference between reactants and products in the CMC reaction, and it is consistent with the reported standard heat of reaction at 298 K (−8.32 eV), justifying the effective use of electronic energy change (ΔE) to approximate the enthalpy change (ΔH) of the reaction. Notably, the order of formation of the proposed intermediates on the surface along with their respective energetics is highly consistent with our experimental observations in the *in situ* DRIFTS analyses both in the preactivation process and the catalytic cycle. Video S2 gives an animated illustration of the full reaction mechanism.

■ CONCLUSIONS

We have found that hematite is an effective catalyst for methane activation, with great potential as an alternative to precious metal catalysts for low temperature combustion of methane into CO_2 and H_2O. We find that the MvK type redox mechanism with participation of the hematite surface oxygen is most consistent with our isotopic oxygen tracer experiments and theoretical analyses. At low temperatures, methane is activated by lattice oxygen rather than by molecular dioxygen from the gas phase. The latter, however, plays a more significant role at higher temperatures, forming a catalytic cycle upon vacancy-promoted molecular dioxygen adsorption. Reaction intermediates were probed by *in situ* DRIFTS and analyzed by DFT calculations at the molecular level. In summary, CH_4 is first dissociatively adsorbed on the lattice oxygens O_{3c} on a tetra-iron center with an antiferromagnetically coupled iron dimer, forming a methoxy CH_3−O species, which then transforms into an adsorbed formate intermediate through both thermal HAT and PCET. A bridging bidentate formate is initially formed, followed by the transition to a monodentate configuration. Finally, CO_2 and H_2O are formed and desorbed, leaving oxygen vacancies on the surface, while other neighboring oxygens both from the lattice and the dioxygen from the gas phase replenish the vacancies and therefore reconstruct the active center. At higher temperatures, CH_4 is activated more favorably by O_2 owing to the vacancy-promoted adsorption of molecular dioxygen, and a complete CMC catalytic cycle is proposed to form on this active vacancy structure.

Hematite, and many other cheap metal oxides, have long been considered mostly as support materials for metal catalysts in many important catalytic reactions, while less exploration of their use as the active component and reaction mechanism has been published. Compared to metal catalysts, many metal oxides can be more readily made into stable high-surface-area materials that are beneficial for surface mechanistic studies, as conducted in this work. This is crucial not only for elucidating the reaction chemistry but also for guiding the next-generation of catalyst design and optimization. In this study particularly, hematite demonstrates great potential in the effective activation of the inert methane molecule at relatively low temperatures (<500 °C). The formation of the stable reaction intermediates also implies future possibilities for upgrading methane to value-added chemicals in heterogeneous catalysis. One example could be to prevent overoxidation of the methoxy and formate species to obtain methanol and formic acid by keeping the reaction temperature lower than 230 °C and extracting the intermediates with proton donors such as water. A hydrophobic surface diffusion layer may help not only the adsorption of the hydrophobic CH_4 reactant but also the desorption of the hydrophilic products such as methanol and formaldehyde to avoid overoxidation. Such a direct route from methane to oxygenated products would be highly desirable for industrial applications due to reduced costs incurred in separation and multiple reaction steps.

■ ASSOCIATED CONTENT

Supporting Information

The Supporting Information is available free of charge at https://pubs.acs.org/doi/10.1021/jacs.0c07179.

Flow reactor setup; complete mass spectra; reaction stoichiometry; blank control test; light-off curve upon a

https://dx.doi.org/10.1021/jacs.0c07179
J. Am. Chem. Soc. 2020, 142, 17119−17130

large mass loading; comparison of typical catalytic systems in CMC; bulk hematite with a large mass loading; postreaction TEM/SEM analyses; XPS analyses; Arrhenius plot; reaction models; TPIOE; self-dehydration in TPR; CH_4-TPR; *in situ* DRIFTS spectra of water desorption and CO_2; models of different hematite facets; self-dehydrated model surface; hydrogen atom parking slabs; CH_4 adsorption on different sites; proposed electron transfer processes; calculated energy barrier of the PCET process; magnetic moment parameters (PDF)

Video S1: Animated molecular vibrations video (MP4)

Video S2: Animated illustration of the proposed full reaction pathway (MP4)

Compiled VASP geometry output files of all calculations (ZIP)

AUTHOR INFORMATION

Corresponding Authors

Ke R. Yang − *Energy Sciences Institute and Department of Chemistry, Yale University, West Haven, Connecticut 06516, United States;* orcid.org/0000-0003-0028-2717; Email: ke.yang@yale.edu

Victor S. Batista − *Energy Sciences Institute and Department of Chemistry, Yale University, West Haven, Connecticut 06516, United States;* orcid.org/0000-0002-3262-1237; Email: victor.batista@yale.edu

Lisa D. Pfefferle − *Department of Chemical and Environmental Engineering, Yale University, New Haven, Connecticut 06520-8286, United States*; Email: lisa.pfefferle@yale.edu

Authors

Yulian He − *Department of Chemical and Environmental Engineering and Energy Sciences Institute, Yale University, New Haven, Connecticut 06520-8286, United States;* orcid.org/0000-0002-8994-1979

Facheng Guo − *Energy Sciences Institute and Department of Chemistry, Yale University, West Haven, Connecticut 06516, United States*

Jake A. Heinlein − *Department of Chemical and Environmental Engineering and Energy Sciences Institute, Yale University, New Haven, Connecticut 06520-8286, United States*

Scott M. Bamonte − *Department of Chemistry, University of Connecticut, Storrs, Connecticut 06269-3060, United States*

Jared J. Fee − *Department of Chemistry, University of Connecticut, Storrs, Connecticut 06269-3060, United States*

Shu Hu − *Department of Chemical and Environmental Engineering and Energy Sciences Institute, Yale University, New Haven, Connecticut 06520-8286, United States;* orcid.org/0000-0002-5041-0169

Steven L. Suib − *Department of Chemistry, University of Connecticut, Storrs, Connecticut 06269-3060, United States;* orcid.org/0000-0003-3073-311X

Gary L. Haller − *Department of Chemical and Environmental Engineering, Yale University, New Haven, Connecticut 06520-8286, United States;* orcid.org/0000-0001-8482-5488

Complete contact information is available at: https://pubs.acs.org/10.1021/jacs.0c07179

Author Contributions

[⊥]Y.H. and F.G. contributed equally to this work.

Notes

The authors declare no competing financial interest.

ACKNOWLEDGMENTS

The authors acknowledge Dr. Michael Rooks at Yale YINQE facilities for providing access to and assistance with TEM and SEM instruments. The authors thank Dr. Min Li at Yale West Campus Materials Characterization Core for assisting with the X-ray Photoelectron Spectrometer. Y.H. thanks Yale Edward L. Barlow Funds for financial support. F.G., K.R.Y., and V.S.B. acknowledge an allocation of high-performance computer time from the National Energy Research Scientific Computing Center (NERSC) and support by the Air Force Office of Scientific Research (AFOSR) grant #FA9550-13-1-0020. The authors also thank the Yale Center for Research Computing for guidance and use of the research computing infrastructure. S.L.S thanks the U.S. Department of Energy Office of Basic Energy Sciences, Division of Chemical, Biological and Geological Sciences under grant DE-FG02-86ER13622.A000 for support of this research.

REFERENCES

(1) Caballero, A.; Pérez, P. J. *Chem. Soc. Rev.* **2013**, *42*, 8809−8820.
(2) Horn, R.; Schlögl, R. *Catal. Lett.* **2015**, *145*, 23−39.
(3) Monai, M.; Montini, T.; Gorte, R. J.; Fornasiero, P. *Eur. J. Inorg. Chem.* **2018**, *2018*, 2884−2893.
(4) Tao, F. F.; Shan, J.-j.; Nguyen, L.; Wang, Z.; Zhang, S.; Zhang, L.; Wu, Z.; Huang, W.; Zeng, S.; Hu, P. *Nat. Commun.* **2015**, *6*, 7798.
(5) Farrauto, R. J. *Science* **2012**, *337*, 659−660.
(6) Eriksson, S. Development of catalysts for natural gas-fired gas turbine combustors, Doctoral Thesis, KTH − Royal Institute of Technology, Stockholm, Sweden, 2006.
(7) Latimer, A. A.; Kakekhani, A.; Kulkarni, A. R.; Nørskov, J. K. *ACS Catal.* **2018**, *8*, 6894−6907.
(8) Chen, J. H.; Arandiyan, H.; Gao, X.; Li, J. H. *Catal. Surv. Asia* **2015**, *19*, 140−171.
(9) Dietl, N.; Schlangen, M.; Schwarz, H. *Angew. Chem., Int. Ed.* **2012**, *51*, 5544−5555.
(10) Zhang, K.; Peng, X.; Cao, Y.; Yang, H.; Wang, X.; Zhang, Y.; Zheng, Y.; Xiao, Y.; Jiang, L. *Mater. Res. Bull.* **2019**, *111*, 338−341.
(11) Yang, J.; Guo, Y. B. *Chin. Chem. Lett.* **2018**, *29*, 252−260.
(12) Popescu, I.; Tanchoux, N.; Tichit, D.; Marcu, I.-C. *Appl. Catal., A* **2017**, *538*, 81−90.
(13) Zhang, L.; Zhang, Y.; Dai, H.; Deng, J.; Wei, L.; He, H. *Catal. Today* **2010**, *153*, 143−149.
(14) Ross, M. O.; Rosenzweig, A. C. *JBIC, J. Biol. Inorg. Chem.* **2017**, *22*, 307−319.
(15) Snyder, B. E.; Bols, M. L.; Schoonheydt, R. A.; Sels, B. F.; Solomon, E. I. *Chem. Rev.* **2018**, *118*, 2718−2768.
(16) Fishman, Z. S.; He, Y.; Yang, K. R.; Lounsbury, A. W.; Zhu, J.; Tran, T. M.; Zimmerman, J. B.; Batista, V. S.; Pfefferle, L. D. *Nanoscale* **2017**, *9*, 12984−12995.
(17) Cornell, R. M.; Schwertmann, U. *The Iron Oxides: Structure, Properties, Reactions, Occurrences and Uses*; John Wiley & Sons, 2003.
(18) Mahyuddin, M. H.; Staykov, A.; Shiota, Y.; Yoshizawa, K. *ACS Catal.* **2016**, *6*, 8321−8331.
(19) Parmaliana, A.; Arena, F.; Frusteri, F.; Martınez-Arias, A.; Granados, M. L.; Fierro, J. *Appl. Catal., A* **2002**, *226*, 163−174.
(20) Schwach, P.; Pan, X.; Bao, X. *Chem. Rev.* **2017**, *117*, 8497−8520.
(21) Mesa, C. A.; Francàs, L.; Yang, K. R.; Garrido-Barros, P.; Pastor, E.; Ma, Y.; Kafizas, A.; Rosser, T. E.; Mayer, M. T.; Reisner, E.; Grätzel, M.; Batista, V. S.; Durrant, J. R. *Nat. Chem.* **2020**, *12*, 82−89.
(22) Sun, L.; Zhan, W.; Li, Y.-A.; Wang, F.; Zhang, X.; Han, X. *Inorg. Chem. Front.* **2018**, *5*, 2332−2339.

(23) Fishman, Z. S.; Rudshteyn, B.; He, Y.; Liu, B.; Chaudhuri, S.; Askerka, M.; Haller, G. L.; Batista, V. S.; Pfefferle, L. D. *J. Am. Chem. Soc.* **2016**, *138*, 10978−85.
(24) Kresse, G.; Furthmüller, J. *Comput. Mater. Sci.* **1996**, *6*, 15−50.
(25) Kresse, G.; Furthmüller, J. *Phys. Rev. B: Condens. Matter Mater. Phys.* **1996**, *54*, 11169−11186.
(26) Kresse, G.; Hafner, J. *Phys. Rev. B: Condens. Matter Mater. Phys.* **1993**, *47*, 558−561.
(27) Kresse, G.; Hafner, J. *Phys. Rev. B: Condens. Matter Mater. Phys.* **1994**, *49*, 14251−14269.
(28) *Jmol: an open-source Java viewer for chemical structures in 3D*. http://www.jmol.org/.
(29) Perdew, J. P.; Burke, K.; Ernzerhof, M. *Phys. Rev. Lett.* **1996**, *77*, 3865−3868.
(30) Kresse, G.; Joubert, D. *Phys. Rev. B: Condens. Matter Mater. Phys.* **1999**, *59*, 1758−1775.
(31) Blöchl, P. E. *Phys. Rev. B: Condens. Matter Mater. Phys.* **1994**, *50*, 17953−17979.
(32) Dudarev, S. L.; Botton, G. A.; Savrasov, S. Y.; Humphreys, C. J.; Sutton, A. P. *Phys. Rev. B: Condens. Matter Mater. Phys.* **1998**, *57*, 1505−1509.
(33) Rollmann, G.; Rohrbach, A.; Entel, P.; Hafner, J. *Phys. Rev. B: Condens. Matter Mater. Phys.* **2004**, *69*, 165107.
(34) Bhowmik, R. N.; Saravanan, A. *J. Appl. Phys.* **2010**, *107*, No. 053916.
(35) Liao, P.; Carter, E. A. *Phys. Chem. Chem. Phys.* **2011**, *13*, 15189−15199.
(36) Berne, B. J.; Ciccotti, G.; Coker, D. F. *Classical and Quantum Dynamics in Condensed Phase Simulations*; World Scientific: Singapore, 1998.
(37) Yu, Q.; Wang, C.; Li, X.; Li, Z.; Wang, L.; Zhang, Q.; Wu, G.; Li, Z. *Fuel* **2019**, *239*, 1240−1245.
(38) Persson, K.; Ersson, A.; Jansson, K.; Iverlund, N.; Järås, S. *J. Catal.* **2005**, *231*, 139−150.
(39) Venezia, A. M.; Di Carlo, G.; Pantaleo, G.; Liotta, L. F.; Melaet, G.; Kruse, N. *Appl. Catal., B* **2009**, *88*, 430−437.
(40) Ciuparu, D.; Lyubovsky, M. R.; Altman, E.; Pfefferle, L. D.; Datye, A. *Catal. Rev.: Sci. Eng.* **2002**, *44*, 593−649.
(41) Cargnello, M.; Jaén, J. J. D.; Garrido, J. C. H.; Bakhmutsky, K.; Montini, T.; Gámez, J. J. C.; Gorte, R. J.; Fornasiero, P. *Science* **2012**, *337*, 713−717.
(42) Yao, Y.-F. Y. *Ind. Eng. Chem. Prod. Res. Dev.* **1980**, *19*, 293−298.
(43) Deng, J.; Zhang, L.; Dai, H.; He, H.; Au, C. T. *Appl. Catal., B* **2009**, *89*, 87−96.
(44) Au-Yeung, J.; Chen, K.; Bell, A. T.; Iglesia, E. *J. Catal.* **1999**, *188*, 132−139.
(45) Zasada, F.; Janas, J.; Piskorz, W.; Gorczyńska, M.; Sojka, Z. *ACS Catal.* **2017**, *7*, 2853−2867.
(46) Kaminski, P. *Arabian J. Chem.* **2020**, *13*, 851−862.
(47) Martin, P. E.; Barker, E. F. *Phys. Rev.* **1932**, *41*, 291.
(48) Scarano, D.; Bertarione, S.; Spoto, G.; Zecchina, A.; Otero Areán, C. *Thin Solid Films* **2001**, *400*, 50−55.
(49) Rotzinger, F. P.; Kesselman-Truttmann, J. M.; Hug, S. J.; Shklover, V.; Grätzel, M. *J. Phys. Chem. B* **2004**, *108*, 5004−5017.
(50) Jung, K.-D.; Bell, A. T. *J. Catal.* **2000**, *193*, 207−223.
(51) Popova, G. Y.; Andrushkevich, T. V.; Chesalov, Y. A.; Stoyanov, E. S. *Kinet. Catal.* **2000**, *41*, 805−811.
(52) Kouva, S.; Honkala, K.; Lefferts, L.; Kanervo, J. *Catal. Sci. Technol.* **2015**, *5*, 3473−3490.
(53) Hu, W.; Lan, J.; Guo, Y.; Cao, X.-M.; Hu, P. *ACS Catal.* **2016**, *6*, 5508−5519.
(54) He, Y.; Yang, K. R.; Yu, Z.; Fishman, Z. S.; Achola, L. A.; Tobin, Z. M.; Heinlein, J. A.; Hu, S.; Suib, S. L.; Batista, V. S.; Pfefferle, L. D. *Nanoscale* **2019**, *11*, 16677−16688.
(55) Luo, Y.-R. *Comprehensive Handbook of Chemical Bond Energies*;. CRC Press, 2007.
(56) Usharani, D.; Lacy, D. C.; Borovik, A. S.; Shaik, S. *J. Am. Chem. Soc.* **2013**, *135*, 17090−17104.
(57) Winkelman, J. G. M.; Voorwinde, O. K.; Ottens, M.; Beenackers, A. A. C. M.; Janssen, L. P. B. M. *Chem. Eng. Sci.* **2002**, *57*, 4067−4076.
(58) Ciuparu, D.; Katsikis, N.; Pfefferle, L. *Appl. Catal., A* **2001**, *216*, 209−215.
(59) Cheng, Z.; Qin, L.; Guo, M.; Xu, M.; Fan, J. A.; Fan, L.-S. *Phys. Chem. Chem. Phys.* **2016**, *18*, 32418−32428.

https://dx.doi.org/10.1021/jacs.0c07179
J. Am. Chem. Soc. 2020, 142, 17119−17130